2026 IEEE International Conference on Robotics and Automation (ICRA 2026)
June 1-5, 2026. Vienna, Austria

Workspace Optimization of a Flexure-Based 3RRR Parallel Robot with Joint Angle Constraints

Annamalai Karuppiah[1] and Ryan Orszulik[1]

***Abstract*—The optimization of flexure-based planar parallel robots with traditional methods demands significant computational resources due to the coupling of kinematic and structural effects. This work presents a decoupled optimization approach, in which the geometry of the manipulator is optimized for workspace via a kinematic model approach. A novel approach is presented via a modified Moore boundary following algorithm which provides for an efficient calculation of the workspace. With this approach, the optimal kinematic design parameters, namely the leg ratio and initial orientation of the end effector are determined and presented for a number of cases described by the combination of joint angle constraints.**

I. Introduction

Mesoscale robotics is an evolving field of research with the intent to design cost-effective and mass producible robots for small-scale manipulation. At small-scales, a sufficiently large range of motion, accuracy, and speed of operation are the three crucial performance objectives to attain a functional robot for applications in alignment of micro-optics elements [1], microassembly [2], and microsurgery [3], [4]. Parallel robots exhibit these characteristics due to their closed-loop structure which improves the mechanical stiffness of the system and allows actuators to be located at the base which reduces the inertia of the robot and results in higher accuracy, speed, acceleration, and load carrying capacity [4]–[6].

However, parallel robots cannot be directly miniaturized as traditional joints impose challenges in the and introduce undesirable phenomena such as wear, backlash, noise, and friction at small scales [7]. A possible solution is the use of compliant mechanisms which allow for a monolithic structure that removes the need for assembly, and eliminates friction and backlash, increasing the precision and reliability of the system. However, the trade-offs are a limited range of motion, parasitic rotation, and reduced load-bearing capacity [8].

To improve the performance of mesoscale parallel robots, piezoelectric bimorph benders can be employed [4], [6] due to their high resolution [9], large bandwidth [10], and favorable scaling properties [11]. With these advantages comes the drawback, a limited range of motion, which is addressed by a compliant transmission mechanism that yields ±30° of rotational motion [10]. For this work, a robot that is monolithically fabricated via additive manufacturing (see Fig. 1) is investigated which offers the advantages of design freedom, rapid prototyping, and cost effectiveness [12], [13].

[1]Annamalai Karuppiah (anna0904@yorku.ca) and Ryan Orszulik (ryan.orszulik@lassonde.yorku.ca) are with the Department of Earth and Space Science and Engineering, York University, Toronto, Canada. This work was supported by the Natural Sciences and Engineering Research Council of Canada.

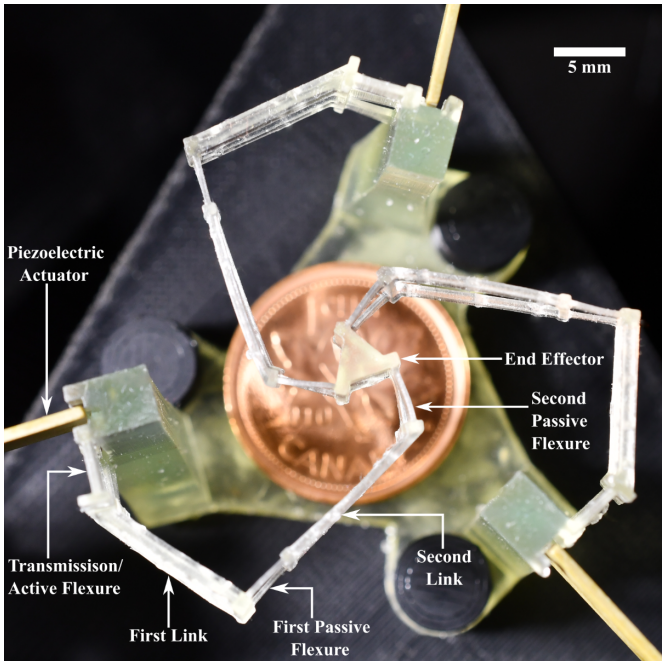

Fig. 1: A prototype of the 3RRR parallel robot fabricated via additive manufacturing next to a Canadian penny (diameter = 19.05 mm).

To maximize the performance of the robot, the design should be optimized for three performance objectives. However, only the flexure properties are typically optimized for workspace [14], [15] while the effect of joint angle constraints are not considered. When the full design was optimized, the focus was on the dynamic performance of the robot within a predetermined target workspace [16]. This work focuses on the first performance objective: large range of motion. The overall system has not yet been optimized specifically in terms of the kinematic parameters of the structure (e.g., leg ratio) has not been considered while considering angle limitations imposed by piezoelectric actuators and compliant joints.

Typically finite element models or the pseudo-rigid body model is used to optimize the design due to the nonlinear nature of compliant mechanisms. However, this yields an optimization problem with a high number of design variables which is complex and requires large computational power. To address this, the paper investigates the kinematic structure of a flexure-based parallel robot in order to allow the optimization of the workspace of the robot to be decoupled to a kinematic and then finite element model problem. This is desirable as it reduces the number of variables that must be considered in the finite

element optimization of the structure to that of the flexure stiffnesses via their geometric parameters (allowing for each flexure to take on a different stiffness) while the kinematic parameters such as leg ratio and initial orientation of the end effector can be considered separately. Here, a kinematic model based optimization is considered for two parameters, namely the leg ratio and initial end effector orientation for a fixed end effector size and robot footprint. The kinematic model sufficiently approximates flexure-based joints as the flexure lengths are significantly smaller than the rigid body lengths (see Fig. 1) hence, the flexure can be modeled as a revolute joint located at the center of the flexure [8] with rotational limits.

This paper studies the 3RRR planar parallel robot which consists of three limbs, each with three links and three revolute joints arranged in plane connecting the fixed base to the moving end-effector (see Fig. 2). The manipulator has three degrees of freedom, namely translation in X- and Y-axis, and rotation about the Z-axis. Every 3RRR manipulator has an associated workspace volume [17] defined by these parameters with units of millimeters squared degrees ($mm^2 \cdot deg$).

The optimal design that maximizes the workspace volume was found to have a leg ratio of one for a 3RRR when active and passive joints have an unlimited range of motion [17]. An optimal kinematic design while considering active and passive joint angle limits that only maximizes the *effective regular workspace* (a workspace that encloses a regular geometrical object, e.g., a square, a circle, a cube, or a sphere) for varying end effector size and robot footprint is presented in [18]. Therefore, the total workspace (i.e., workspace volume) optimization problem should be revisited to find an optimal kinematic design while accounting for active and passive joint angle limits to achieve the first performance objective. To identify the optimal kinematic design that maximizes the workspace volume, the workspace for a given design has to be calculated accurately and efficiently. The workspace calculation methods were summarized and categorized into geometrical, numerical, and discretization-based [19].

The geometrical method is implemented by establishing a geometrical object for each limb of the manipulator. Geometrical objects include a set of concentric circles, spheres, or cylinders that depend on the types of joints in the manipulator. This approach is fast and reliable and it provides a minimal representation of the workspace volume in a geometric form [19]. This method was investigated via an analytical implementation [17]. However, the main drawback of this method is, it is difficult to consider kinematic constraints [19].

The numerical method is executed by devising algebraic equations and using numerical solution techniques to compute the workspace boundaries. Some examples of this method are, the Jacobian based [20], tangent vector based [21], optimization [22], zero velocity based [23], [24], interval analysis [25], and stratified layer based [26] approaches. The major drawback of employing numerical methods for this work is the complexity involved in the analysis due to the possibility of non-convex workspace polygons.

In discretization-based methods, each point of a grid is tested for the workspace condition. The workspace condition is defined by whether a point is a singularity and if the pose is within the allowable active and passive joint angle limits. Typically, the choice of the grid is a box grid [27] in Cartesian coordinates while polar grids can also be used [19]. While discretization-based methods easily allow the consideration of constraints, the approach is computationally intensive. That is the accuracy of the workspace depends on the granularity of the grid and the computational time scales exponentially with the step size [19]. A few examples of this approach include the workspace quantization of a seven degrees-of-freedom parallel robot [28], a serial-parallel hybrid leg [27], and a Delta robot [29] while accounting for joint angle limits.

Therefore, the methods of workspace analysis can be ranked in the increasing order of both versatility and computational cost as follows; geometrical methods offer little to no flexibility but provide a fast, accurate, and minimal representation of the workspace volume, while numerical methods allow one to consider most of the constraints with minimal demand on computational resources, however the process of introducing new constraints is rather difficult due to the need to derive complex algebraic equations. Lastly, discretization offers significant freedom and ease of adoption but with a significant requirement for computational resources and runtime to produce a sufficiently accurate analysis.

Hence a novel method that incorporates constraints and remains easy to adopt therefore leveraging the benefits of both numerical and discretization-based methods is proposed in this work. The discretization-based approach is adopted and instead of evaluating every single Cartesian point, the workspace boundary is directly evaluated with the Moore boundary tracing algorithm [30] to address the large demand on computational resources and runtime. This enables the optimization study to search through a large design space to identify the optimal parameters that maximizes the workspace volume.

II. Workspace Calculation Methodology

Boundary/ border following algorithms are vital in the digital image processing field for feature extraction of grayscale images [30]. It is used to derive a sequence of coordinates or chain codes between a connected set of 1-pixels and a connected set of 0-pixels [31].

Here, the Moore algorithm is employed for the workspace boundary determination problem with certain modifications. The pixels are replaced with Cartesian points (x, y) and a 1-pixel is defined as a workspace point and a 0-pixel is defined as a point outside the workspace. For a given end effector orientation ϕ the planar workspace slab of the manipulator in (x, y) is calculated and this is repeated for all discrete end effector orientations. The logic behind the approach is to start at a known workspace point (x, y, ϕ) on the boundary as the center point of a 3×3 grid and search the 8 neighboring points that are at located at a desired distance (in this work 50 μm) to identify the next workspace point. The iteration terminates when the search point reaches the initial workspace point. Since this approach directly operates on kinematic equations it can

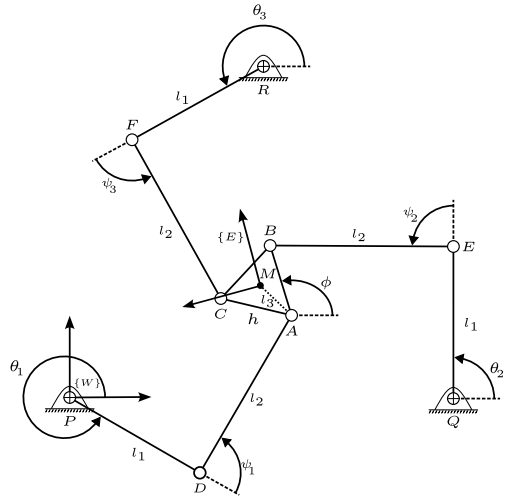

Fig. 2: Kinematic diagram of a symmetric 3RRR manipulator.

be extended to analyze workspaces of 4-, 5-, and 6- DOF manipulators.

In this work, the manipulator is designed for no specific task, hence it is assumed to be symmetric [17]. The architecture of a symmetric manipulator is characterized by leg ratio $l_r = \frac{l_1}{l_2}$ (see Fig. 2) and initial end effector (EE) orientation ϕ_{ini}. The leg ratio is the ratio between the first link l_1 and second link l_2 of a limb. A point in the three-degree-of-freedom space (x, y, ϕ) qualifies as a workspace point if the active and passive joint angles at this configuration are within the desired joint angle limits and if the manipulator configuration is non-singular.

With this workspace calculation method, a search is performed on a piece-wise continuous grid of plausible architecture paramaters, leg ratio and initial end effector orientation to optimize the workspace volume subject to active and passive joint angle limits. Consequently, the active and passive joint angles need to be calculated which is performed by establishing the kinematics of the manipulator. The kinematics of a parallel robot are categorized into inverse (IK) and forward kinematics (FK) [5]. For parallel robots the IK is known to have closed-form solutions and the FK is typically solved numerically. As a result in this work IK is employed as it can be solved easily.

To derive IK, first, the geometry of the manipulator has to be defined (see Fig. 2), which is given by points P, Q, R that correspond to the active joints, D, E, F that correspond to the first passive joint in the three limbs, A, B, C that correspond to the second passive joint or the vertices of the end effector and M which is the midpoint of the end effector. The length of the first, second and third links of all three limbs are denoted by l_1, l_2, and l_3 due to the symmetric nature. The active joints P, Q, R form an equilateral triangle $\triangle PQR$ which is known as the robot footprint. The points A, B, C form an equilateral triangle $\triangle ABC$ which is defined as the end effector (EE) with a median of length l_3. The length of the side of $\triangle ABC$ is given by h. The active joint angle θ_i is established and limited by the piezoelectric actuators and the transmission, ψ_i is the first, and ϕ is the second passive joint angle limited by the compliant flexures for the i^{th} limb where $i = 1, 2, 3$, for the 3RRR.

A. Inverse Kinematics

Inverse kinematics calculates the active joint angles denoted as $\theta_1, \theta_2, \theta_3$ for the desired midpoint position x_m, y_m and orientation angle ϕ.

1) Active Joint Angle Calculation: The angle of the i^{th} active joint θ_i can be calculated as

$$\theta_i = 2\arctan\frac{-e_1 \pm \sqrt{e_{i1}^2 + e_{i2}^2 - e_{i3}^2}}{e_{i3} - e_{i2}} \tag{1}$$

where e_1, e_2, e_3 for limb 1 are given by

$$\begin{aligned} e_{11} &= 2y_P l_1 - 2y_A l_1 \\ e_{12} &= 2x_P l_1 - 2x_A l_1 \\ e_{13} &= x_A^2 + y_A^2 + x_P^2 + y_P^2 + l_1^2 - l_2^2 - 2x_A x_P - 2y_A y_P \end{aligned} \tag{2}$$

for limb 2 are given by

$$\begin{aligned} e_{21} &= 2y_Q l_1 - 2y_A l_1 - 2l_1 h\sin\phi \\ e_{22} &= 2x_Q l_1 - 2x_A l_1 - 2l_1 h\cos\phi \\ e_{23} &= x_A^2 + y_A^2 + x_Q^2 + y_Q^2 + h^2 + l_1^2 - l_2^2 - 2x_A x_Q - 2y_A y_Q \\ &\quad + 2x_A h\cos\phi + 2y_A h\sin\phi - 2x_Q h\cos\phi - 2y_Q h\sin\phi \end{aligned} \tag{3}$$

and for limb 3 are given by

$$\begin{aligned} e_{31} &= 2y_R l_1 - 2y_A l_1 - 2l_1 h\sin\left(\phi + \frac{\pi}{3}\right) \\ e_{32} &= 2x_R l_1 - 2x_A l_1 - 2l_1 h\cos\left(\phi + \frac{\pi}{3}\right) \\ e_{33} &= x_A^2 + y_A^2 + x_R^2 + y_R^2 + h^2 + l_1^2 - l_2^2 - 2x_A x_R - 2y_A y_R \\ &\quad + 2x_A h\cos\left(\phi + \frac{\pi}{3}\right) + 2y_A h\sin\left(\phi + \frac{\pi}{3}\right) \\ &\quad - 2x_R h\cos\left(\phi + \frac{\pi}{3}\right) - 2y_R h\sin\left(\phi + \frac{\pi}{3}\right) \end{aligned} \tag{4}$$

in which x_P, y_P is the coordinate of point P (and similarly for other points Q, R, and A).

With the kinematics, the home configuration of a given architecture is characterized by the IK solutions that correspond to the unactuated case, where the EE point M is located at the centroid of the robot footprint $\triangle PQR$. This IK solution is stored as the initial active joint angles $\theta_{i_{ini}}$. The IK solution from the home configuration for any non-zero Cartesian and EE rotation $\mathbf{x} = [\Delta x, \Delta y, \Delta\phi]^T$ is treated as the active joint angle solution $\theta_{i_{sol}}$. The active joint angle rotation is then defined as $\Delta\theta_i = (\theta_{i_{sol}} - \theta_{i_{ini}})$.

Note that Eq. (1) yields 8 sets of solutions. Only two sets of solutions result in a symmetric manipulator, namely, when the $\pm$ is + or − for all θ_i. In this work, the choice is − for all θ_i due to the initial configuration chosen for the robot. With the active joint angles calculated, the first passive joint angles can now be calculated.

2) First Passive Joint Angle Calculation: The angle of the i^{th} first passive joint ψ_i can be calculated as

$$\psi_1 = \arctan\left(\frac{y_A - y_P - l_1\sin\theta_1}{x_A - x_P - l_1\cos\theta_1}\right) - \theta_1 \tag{5}$$

$$\psi_2 = \arctan\left(\frac{y_A - y_Q - l_1\sin\theta_2 + h\sin\phi}{x_A - x_Q - l_1\cos\theta_2 + h\cos\phi}\right) - \theta_2 \tag{6}$$

$$\psi_3 = \arctan\left(\frac{y_A - y_R - l_1 \sin\theta_3 + h\sin\left(\phi + \frac{\pi}{3}\right)}{x_A - x_R - l_1\cos\theta_3 + h\cos\left(\phi + \frac{\pi}{3}\right)}\right) - \theta_3 \quad (7)$$

Similar to the active joint angle rotation calculation, the passive joint angle rotation is defined as $\Delta\psi_i = (\psi_{i_{sol}} - \psi_{i_{ini}})$. The kinematics of the manipulator is fully known, hence singular configurations can be easily identified.

B. Singularity Analysis

A robot configuration is characterized by active joint angle rotation, $\Delta\theta_i$, passive joint angle rotation, $\Delta\psi_i$, EE translational displacement, Δx, Δy, and EE rotation $\Delta\phi$ from the home configuration of a given architecture. Singular configurations occur when the Jacobian matrix becomes rank deficient [32]. The manipulator system Jacobian matrix J, which is configuration dependent, can be separated into two matrices, one corresponding to the IK Jacobian, J_q and the other to the FK Jacobian, J_x [33]. The Jacobian matrices are derived via the time derivatives of the vector-loop closure equations [5]. Hence the Jacobian matrices establish a relationship between the joint velocities and the EE velocities as follows

$$J_q\dot{\mathbf{q}} = J_x\dot{\mathbf{x}} \quad (8)$$

where $\dot{\mathbf{q}} = [\dot{\theta}_1, \dot{\theta}_2, \dot{\theta}_3]^T$ is the active joint velocities, and $\dot{\mathbf{x}} = [\dot{x}_m, \dot{y}_m, \dot{\phi}]^T$ is the translational and rotational velocity of the EE. Since the 3RRR is a fully actuated manipulator, the forward and inverse Jacobian are square 3×3 matrices, defined as

$$J_q = \begin{bmatrix} a_{1x}b_{1y} - a_{1y}b_{1x} & 0 & 0 \\ 0 & a_{2x}b_{2y} - a_{2y}b_{2x} & 0 \\ 0 & 0 & a_{3x}b_{3y} - a_{3y}b_{3x} \end{bmatrix} \quad (9)$$

$$J_x = \begin{bmatrix} b_{1x} & b_{1y} & e_{1x}b_{1y} - e_{1y}b_{1x} \\ b_{2x} & b_{2y} & e_{2x}b_{2y} - e_{2y}b_{2x} \\ b_{3x} & b_{3y} & e_{3x}b_{3y} - e_{3y}b_{3x} \end{bmatrix} \quad (10)$$

where $\mathbf{a}_i$, $\mathbf{b}_i$, and $\mathbf{e}_i$ denote the vectors of the first, second, and third link of the i^{th} limb. The $\mathbf{a}_i$ vector originates at P, Q, or R and goes to D, E, or F corresponding to i^{th} limb. Similarly vector $\mathbf{b}_i$ originates at D, E, or F and goes to A, B, or C. The vector $\mathbf{e}_i$ originates at M and goes to A, B, or C.

The rank deficiency is identified by checking if the inverse Jacobian is singular, $\det(J_q) = 0$ resulting in a type 1 or IK singularity. Similarly if $\det(J_x) = 0$, a type 2 or FK singularity occurs, and if both Jacobians are singular $\det(J_q) = 0$ and $\det(J_x) = 0$, a type 3 or combined singularity is observed [5].

Hence, the tools to qualify a workspace point have been defined. With this, the workspace boundary for a given EE orientation ϕ, referred to as a workspace slab shall be established.

C. Workspace Slab Definition

A workspace slab is defined as the planar workspace boundary in Cartesian coordinates for a fixed EE orientation ϕ. The planar workspace boundary (see Fig. 3a) is defined by the maximum achievable displacements along the X- and Y-axis, Δx and Δy. Consequently, for a given architecture defined by leg ratio l_r and initial EE orientation ϕ_{ini}, and for a given

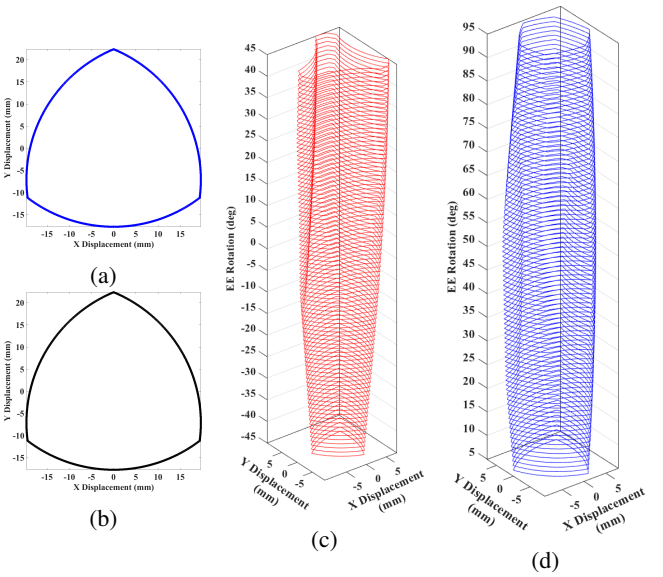

Fig. 3: Generation of a single workspace slab via (a) an exhaustive box grid search approach and (b) the modified Moore boundary following search approach. Computed workspace volume results for (c) architecture with $l_r = 1$ and $\phi_{ini} = 0°$, results in a joint angle limited workspace volume of 12816.67 $mm^2 \cdot$ deg and for (d) architecture with $l_r = 1$ and $\phi_{ini} = 50°$, yields a joint angle limited workspace volume of 15607.04 $mm^2 \cdot$ deg.

EE rotation $\Delta\phi$, a workspace slab is generated if and only if the EE rotation is within the allowable EE rotation limits $\Delta\phi_{min} \leq \Delta\phi \leq \Delta\phi_{max}$, where $\Delta\phi_{min}$ and $\Delta\phi_{max}$ are the minimum and maximum EE rotation limits. Additionally for each slab, a point qualifies as a workspace point if and only if the active and passive joint angle rotations are within the specified joint angle rotation limits $\Delta\theta_{min} \leq \Delta\theta_i \leq \Delta\theta_{max}$ and $\Delta\psi_{min} \leq \Delta\psi_i \leq \Delta\psi_{max}$, and the configuration is non-singular $\det(J_q) \neq 0$ and $\det(J_x) \neq 0$.

Note that this Moore algorithm only considers external singularities since the determinants are checked solely around the boundary. A modified implementation accounts for internal isolated IK singularities by checking if a motor point (P,Q, or R) is in the workspace polygon and subtracting the singular region area from the workspace slab area. For an architecture with a leg ratio of one and an initial EE orientation of 0°, the exhaustive grid search (see Fig. 3a) and the modified Moore boundary following search (see Fig. 3b) results are compared for an identical search grid setup. The exhaustive grid search requires a post-processing step, namely, polygon fitting where the convex hull of the points are identified. However, the Moore approach directly calculates the boundary and is able to accurately identify non-convex polygons [30]. The workspace area of the slab from both approaches are identical at 1171.53 mm^2, while the modified Moore approach is 50 times faster.

Generating and arranging these workspace slabs for varying EE rotations yield the workspace volume of the 3RRR manipulator.

D. Workspace Volume Definition

The workspace volume W was introduced to represent the total workspace of the robot in all three-degree-of-freedom in millimeters squared degrees or millimeters squared radians [17]. The workspace volume can be defined via the discrete integration of workspace slabs with Simpson's rule. In [17] the workspace slabs are discretized along the EE orientation direction ϕ from 0° to 360°. This definition is modified here to introduce the initial EE orientation ϕ_{ini} and EE rotation $\Delta\phi$ parameters by altering the discretization limits to [-180°,180°]. The modified workspace volume is defined as

$$W = \int_{-\pi}^{\pi} A(\phi)d\phi \approx \frac{\delta\phi}{3}[A_0 + 4A_1 + 2A_2 + \cdots + 4A_{2n-1} + A_{2n}] \tag{11}$$

where

$$A_j = A(\phi_{ini} + j\delta\phi),\ \delta\phi = \frac{\pi}{n},\ j = -n, \ldots, 0 \ldots, n \tag{12}$$

and A_j is the area of the workspace slab for $\phi = \phi_{ini} + \phi_j = \phi_{ini} + j\delta\phi = \Delta\phi$. Similar to the modified Moore algorithm setup for workspace slab, n can be understood as the angular discretization parameter, which is chosen to be π or 180° for this implementation, thus the EE rotation is discretized into 1° slabs. Therefore, for a given architecture, the workspace volume is evaluated by generating workspace slabs for all discretized EE rotations.

The maximization of this workspace volume definition is the objective of this optimization to identify the best possible architecture subject to joint angle constraints.

III. 3RRR Architecture Optimization

Traditionally, the architecture of the 3RRR manipulator has been defined only by leg ratio as the joints enjoy full freedom of motion. Hence previous work focused on identifying an optimal leg ratio. However, here it is shown that a new parameter, the initial end effector orientation ϕ_{ini} emerges when joint angle constraints are considered.

To demonstrate the importance of ϕ_{ini}, an arbitrary set of symmetric joint angle rotation limits are chosen, $|\Delta\theta_i| \leq 30°$, $|\Delta\psi_i| \leq 45°$, and $|\Delta\phi| \leq 45°$. For these limits, two architectures with identical leg ratio and varying initial EE orientation are investigated to determine if the initial EE orientation affects the computed workspace volume. As shown in Fig. 3c and Fig. 3d, varying the initial EE orientation by 50° results in an increase in workspace volume of more than 2500 $\text{mm}^2 \cdot \text{deg}$, from 12816.67 $\text{mm}^2 \cdot \text{deg}$ to 15607.04 $\text{mm}^2 \cdot \text{deg}$. This indicates that the initial EE orientation should be considered as a design parameter for the general problem of optimizing the workspace volume of a 3RRR manipulator under joint angle constraints. Hence, the design space for the optimization problem is defined by the leg ratio and the initial EE orientation.

A. Optimization Problem

The optimization problem to maximize the workspace volume of the 3RRR manipulator is formulated as

$$\begin{aligned} &\text{maximize } W(l_r, \phi_{ini}) \\ &\text{subject to } \Delta\theta_{min} \leq \Delta\theta_i \leq \Delta\theta_{max} \\ &\qquad \Delta\psi_{min} \leq \Delta\psi_i \leq \Delta\psi_{max} \\ &\qquad \Delta\phi_{min} \leq \Delta\phi \leq \Delta\phi_{max} \end{aligned} \tag{13}$$

Thus, the problem is to identify the optimal architecture (leg ratio $l_r = \frac{l_1}{l_2}$ and initial EE orientation ϕ_{ini}) under a given set of joint angle rotation constraints, namely, active joint angle rotation limits $[\Delta\theta_{min}, \Delta\theta_{max}]$, first passive joint angle rotation limits $[\Delta\psi_{min}, \Delta\psi_{max}]$ and second passive joint angle rotation limits $[\Delta\phi_{min}, \Delta\phi_{max}]$. This optimization problem is solved for a given robot footprint, end effector size, and total limb length resulting in geometric constraints, $|\mathbf{PQ}| = |\mathbf{QR}| = |\mathbf{RP}| = 32$ mm, $l_3 = 4.25$ mm, and $l_1 + l_2 = 32$ mm (see Fig. 2). The optimization problem is solved with a search by evaluating the workspace volume on the search space $l_r = [0.5, 0.6, \ldots, 2.5]$ and $\phi_{ini} = [-180°, -179°, \ldots, 0, \ldots, 179°, 180°]$. Hence, at each node in the search grid, that is, for a given leg ratio and initial EE orientation, the workspace volume is generated by computing individual workspace polygon slabs discretely for all EE orientations in the region, $\phi_{ini} - \Delta\phi_{min} \leq \phi \leq \phi_{ini} + \Delta\phi_{max}$. For example, if $\phi_{ini} = 0°$, and $\Delta\phi_{min} = -45°$ and $\Delta\phi_{max} = 45°$ (with increments of 1°), 91 workspace polygon slabs will be generated (see Fig. 3c) and the total workspace volume is calculated with Eq. (11). Parallel computing is leveraged to search the vast search space efficiently.

To properly characterize the significance of joint angle rotation limits on the optimal architecture parameters, one joint angle rotation limit is symmetrically (i.e., $\Delta\theta_{min} = -\Delta\theta_{max}$, $\Delta\psi_{min} = -\Delta\psi_{max}$, and $\Delta\phi_{min} = -\Delta\phi_{max}$) varied at a time for 15° increments in the range $[0°, 180°]$ while the other two joint angle rotation limits remain unconstrained. This is done as the active, first, and second passive joint angle limits would be determined for a flexure-based parallel robot by the stress for a particular flexure design and the yield strength of the flexure material.

B. Results and Discussion

The workspace volume against active joint angle rotation limits for optimal architectures is presented in Fig. 4a, against first passive joint angle rotation limits in Fig. 4b, and against second passive joint angle rotation limits in Fig. 4c. Note that for the first and second case, for each limit, 2606420 workspace slabs were generated and analyzed to determine the optimal architectures. The common trend observed among the three plots is the increase in workspace volume as the joint angle rotation limit is increased, as expected since an increase in the joint angle rotation limit results in a larger allowable motion of the link.

1) Varying Active Joint Angle Rotation Limits With Unconstrained First and Second Passive Joints: First, for small active joint angle rotation limits, the optimal leg ratio starts

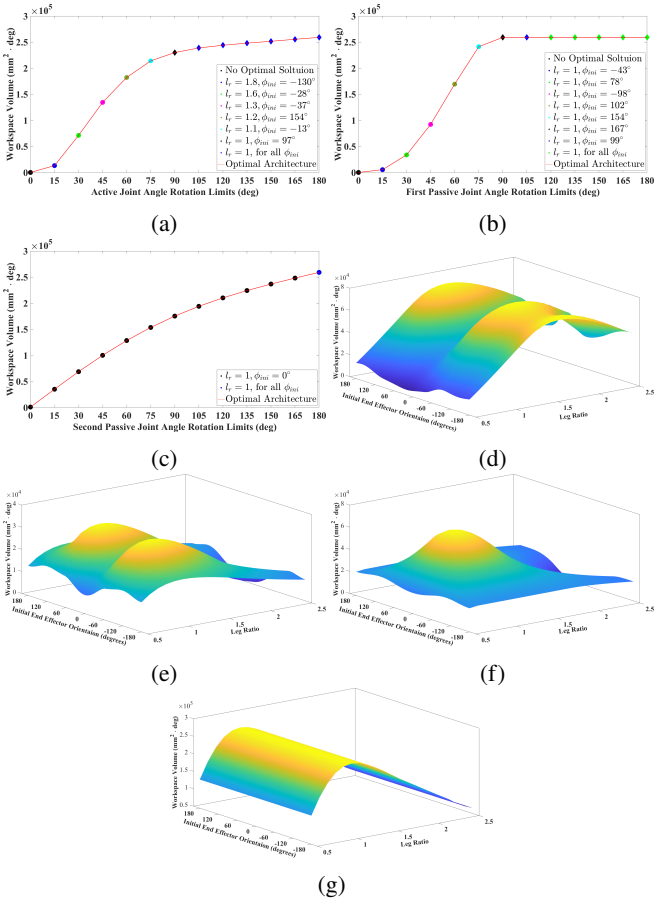

Fig. 4: Architecture optimization results. (a) Workspace volume versus active joint angle rotation limits. (b) Workspace volume versus first passive joint angle rotation limits. (c) Workspace volume versus second passive joint angle limits. Optimal architecture surface, (d) for active joint angle rotation limits, $|\Delta\theta_i| \leq 30°$, (e) for first passive joint angle rotation limits, $|\Delta\psi_i| \leq 30°$, (f) for second passive joint angle rotation limits, $|\Delta\phi| \leq 30°$, and (g) for unconstrained joint angles.

at 1.8 and approaches the optimal solution of 1 for an unconstrained active joint [17] as presented in Fig. 4a. A clear trend could not be established for the workspace volume versus initial EE orientation relationship. The expected cause is due to the fact that the optimal setup for a given set of joint angle limits is characterized by a single numerical maximum for workspace volume. However, observing Fig. 4d indicates that multiple local maxima exist along a line of optimal leg ratio. That is, more than one architecture with identical leg ratio but different initial EE orientations emerge as optimal solutions. For certain combinations of joint angle rotation limits, the optimal architecture based on the numerical maximum results in physical crossover between links and the EE. Since the flexure-based parallel robot is fabricated monolithically, a coplanar design is adopted, that is the links and EE are fabricated in the same plane. Therefore, the architecture that maximizes the computed workspace volume and does not portray a physical crossover is chosen as the optimal and feasible setup.

Second, as the active joint angle limits approach 180°, the significance of initial EE orientation decreases. This local trend is evident when observing the workspace volume versus the architecture search grid results for symmetric active joint angle limits of 30° (see Fig. 4d) and for unconstrained active joint angles (see Fig. 4g). As seen in Fig. 4d, two local maxima are seen for the general optimization problem gradually approaching a single global solution for the unconstrained case as shown in Fig. 4g. Specifically, for small joint angle limits two or more workspace volume peaks are observed, and as the joint angle limits increases, the peaks combine to yield a single optimal solution.

Lastly, the workspace volume gradually increases and attains a peak when the angles are unconstrained as shown in Fig. 4a. Additionally, active joint angle rotation limits result in the largest variation in the optimal architecture parameters from $l_r = 1.8, \phi_{ini} = -130°$ for $|\Delta\theta_i| \leq 15°$ to $l_r = 1$, for all ϕ_{ini} for $|\Delta\theta_i|$ unconstrained, which implies that the active joint angle limits are, unsurprisingly, the most significant.

The optimal solution for active joint angle rotation limits of $|\Delta\theta_i| \leq 30°$ is $l_r = 1.6$ and $\phi_{ini} = -28°$ is depicted in Fig. 5a and the optimal solution of $l_r = 1$ and $\phi_{ini} = 0°$ from [17] is depicted in Fig. 5c. Note that, in [17], ϕ_{ini} was not considered as an architecture parameter as the joints were unconstrained, and as stated above, for the unconstrained case any ϕ_{ini} is an optimal setup with $l_r = 1$ and can be chosen as 0° for convenience with the reference solution with $l_r = 1$.

For the setup in Fig. 5a, the first links are significantly longer than the second links due to the active joint angle rotation constraint imposed. The active joint angle rotation limits are counteracted by the large first link length, therefore maintaining a large first link stroke. The computed workspace volume for the optimal setups from this work and with the reference solution is shown in Fig. 6a. Numerically, the optimal setup from this work yielded almost double the computed workspace volume with $l_r = 1.6$ and $\phi_{ini} = -28°$ (see Fig. 5a) which resulted in $W = 71055.75\ \text{mm}^2\cdot\text{deg}$ and the reference solution architecture with $l_r = 1$ and $\phi_{ini} = 0°$ (see Fig. 5c) resulted in $W = 37200.46\ \text{mm}^2\cdot\text{deg}$. Visually, the workspace slabs of the optimal solution found here encompasses the reference solution as shown in Fig. 6a.

2) Varying First Passive Joint Angle Rotation Limits With Unconstrained Active, and Second Passive Joints: The optimal leg ratio in this case does not vary from one however the initial EE orientation varies as seen in Fig. 4b. Hence the leg ratio does not depend on first passive joint angle rotation limits from the results. Furthermore, unlike the active joint angle rotation limit case, the workspace volume peaks at first passive joint angle rotation limits of 90° and remains consistent for limits above this as shown in Fig. 4b.

Locally, for symmetric first passive joint angle rotation limits of 30° (see Fig. 4e), two exact optimal solutions always emerge for all the considered limits, unlike the active joint angle limit case where more than two solutions emerge and the number of solutions varies with the limits. Note that these solutions have the same leg ratio but symmetric initial EE orientation values.

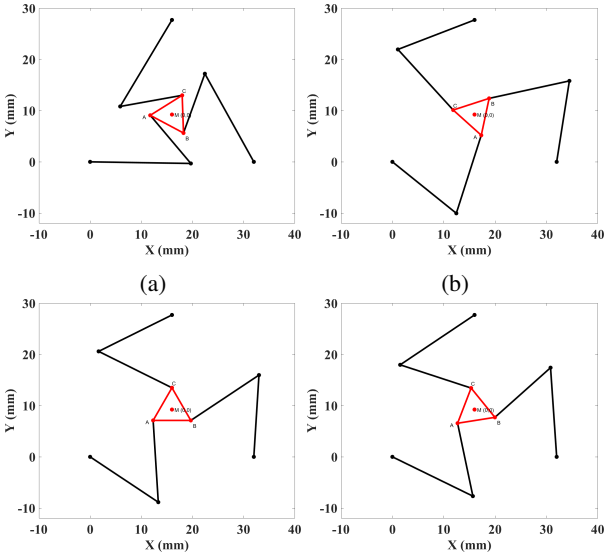

Fig. 5: Depiction of the optimal kinematic architecture for (a) active joint angle rotation limits of $|\Delta\theta_i| \leq 30°$ and other two joints unlimited, with $l_r = 1.6$ and $\phi_{ini} = -28°$, (b) first passive joint angle rotation limits of $|\Delta\psi_i| \leq 30°$ and other two joints unlimited, with $l_r = 1$ and $\phi_{ini} = 78°$, (c) reference solution or second passive joint angle rotation limits of $|\Delta\phi| \leq 30°$ and other two joints unlimited, with $l_r = 1$ and $\phi_{ini} = 0°$, and (d) is the final design when all three joint angle rotations are limited to $\pm 30°$, resulting in $l_r = 1.2$ and $\phi_{ini} = 9°$.

That is the peaks in Fig. 4e are symmetric about $\phi_{ini} = 0°$. For small joint angle limits, the optimal solutions are closer to $\phi_{ini} = 0°$ and gradually spread out towards either end of the Y-axis (initial EE orientation) (for an example see Fig. 4e) until the symmetric joint angle limit is at 105°. As the limit approaches the unconstrained case, the surface unfolds into a single global solution which is shown in Fig. 4g.

The optimal kinematic architecture solution for the first passive joint angle rotation limit of $|\Delta\psi_i| \leq 30°$ is $l_r = 1$ and $\phi_{ini} = 78°$ and is presented in Fig. 5b which is compared against the reference solution architecture depicted in Fig. 5c. The comparison is made by observing the workspace volume as shown in Fig. 6b. Numerically, the optimal setup found here yielded a computed workspace volume of $W = 33664.47\ \text{mm}^2 \cdot$ deg in comparison to the workspace volume of the reference solution of $W = 21493.19\ \text{mm}^2 \cdot$deg. Importantly, note that the reference solution allows EE rotations of $\Delta\phi = [-123°, 123°]$ while the optimal setup found here can manipulate across the full range of EE rotations $\Delta\phi = [-180°, 180°]$ as shown in Fig. 6b.

3) Varying Second Passive Joint Angle Rotation Limits With Unconstrained Active, and First Passive joints: The second passive joint angle rotation limit appears to be the least relevant with regards to the optimal architecture. As shown in Fig. 4c, the optimal architecture remains consistent for all tested joint angles at a leg ratio of 1 and an initial EE orientation of 0°. Additionally, the workspace volume gradually increases

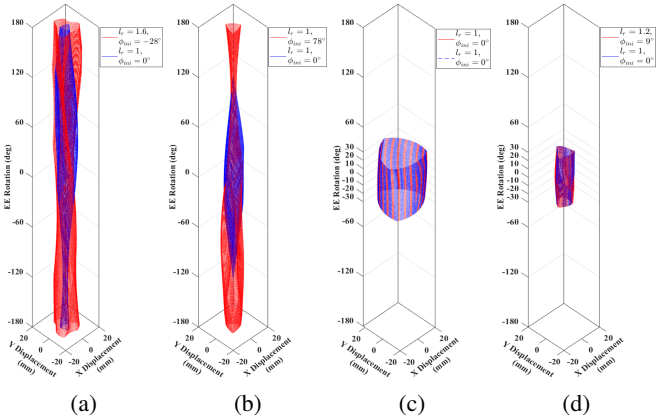

Fig. 6: Comparison of computed workspace volume of the reference solution versus the optimal architecture found here: (a) with active joint angle rotation limits of $|\Delta\theta_i| \leq 30°$ and other two joints unlimited, (b) with first passive joint angle rotation limits of $|\Delta\psi_i| \leq 30°$ and other two joints unlimited, (c) with second passive joint angle rotation limits of $|\Delta\phi| \leq 30°$ and other two joints unlimited, and (d) with all three joint angle rotations limited to $\pm 30°$.

and peaks at the unconstrained case as shown in Fig.4c.

Upon closer inspection of Fig. 4f, only a single optimal solution emerges for all tested rotation limits. The surface presented in Fig. 4f is consistently maintained throughout all joint angle rotation limits until the last unconstrained case which results in Fig. 4g. The optimal kinematic architecture solution for second passive joint angle rotation limit of $|\Delta\phi| \leq 30°$ is identical to the reference solution with $l_r = 1$ and $\phi_{ini} = 0°$ as depicted in Fig. 5c. Consequently, the computed workspace volume is identical at $W = 68595.17\ \text{mm}^2 \cdot$ deg as shown in Fig. 6c.

Thus, from the variation seen in the optimal architecture parameters and the gain in workspace volume, the active joint angle rotation limits emerge as the most significant constraint in this study.

4) Implementation for a Flexure-Based Parallel Robot: The active joint angle rotation is limited by the achievable rotation with the piezoelectric actuator through the compliant transmission to $\pm 30°$ [10]. The other two constraints, namely the first and second passive joint angle rotation limits are assumed to be identical to the active joint angle rotation limits for this study as an assumption.

Therefore, the optimization problem is solved for a flexure-based parallel robot, in which, the joint angle rotation constraints are limited to $\Delta\theta_{min} = \Delta\psi_{min} = \Delta\phi_{min} = -30°$ and $\Delta\theta_{max} = \Delta\psi_{max} = \Delta\phi_{max} = 30°$. The workspace optimization generates 440420 workspace slabs and produces an optimal architecture with $l_r = 1.2$ and $\phi_{ini} = 9°$ with a computed workspace volume of 9191.08 $\text{mm}^2 \cdot$ deg. The workspace volume is compared against the reference solution which yields a workspace volume of 8342.29 $\text{mm}^2 \cdot$ deg as shown in Fig. 6d. Hence, an improvement of approximately 850 $\text{mm}^2 \cdot$ deg is observed in the workspace volume from this

optimization framework for a flexure-based parallel robot.

IV. Conclusion

Parallel robots with flexure joints result in significantly reduced rotations of the robot joints. In particular driving the robot through a flexure-based transmission mechanism with piezoelectric actuators. This necessitates optimizing the robot structure to achieve the largest total workspace. Here, a novel and efficient planar workspace evaluation method based on a modified Moore boundary following algorithm is presented.

The joint angle rotation limits imposed revealed that the initial EE orientation has to be considered as a design parameter for the optimization of the workspace volume. With this, the manipulator architecture is optimized through a search on leg ratio and initial EE orientation while considering active and passive joint angle limits. The joint angle limits, in order of relevance to the optimal architecture parameters are, the active joint angle limits, followed by the first passive joint angle limits, and lastly the second passive joint angle limits. This conclusion is adopted for a flexure-based parallel robot by assuming identical limits for all three joints and the final optimal architecture of a 3$\underline{\text{R}}$RR flexure-based parallel robot was determined to have a leg ratio of 1.2, an initial EE orientation of 9° with an increase in workspace volume of 850 $\text{mm}^2 \cdot \text{deg}$ over the reference solution.

Future works, includes better characterizing the relationship between joint angle rotation limits and optimal architecture parameters, optimizing on the tradeoff against natural frequency, and alternative performance metrics.

References

[1] Y. Bellouard, *Microrobotics: Methods and Applications*. CRC Press, 2009.

[2] R. Zhang, A. Sherehiy, D. Wei, and D. O. Popa, "Design and characterization of solid articulated four axes microrobot for microfactory applications," *Journal of Micro-Bio Robotics*, vol. 15, pp. 119–131, Jun. 2019.

[3] J. E. Correa, J. Toombs, N. Toombs, and P. M. Ferreira, "Laminated micro-machine: Design and fabrication of a flexure-based delta robot," *Journal of Manufacturing Processes*, vol. 24, pp. 370–375, Oct. 2016.

[4] H. McClintock, F. Z. Temel, N. Doshi, J.-s. Koh, and R. J. Wood, "The milliDelta: A high-bandwidth, high-precision, millimeter-scale Delta robot," *Science Robotics*, vol. 3, no. 14, p. eaar3018, Jan 2018.

[5] L.-W. Tsai, *Robot Analysis: The Mechanics of Serial and Parallel Manipulators*. John Wiley & Sons Ltd., 1999.

[6] M. Leveziel, W. Haouas, G. J. Laurent, M. Gauthier, and R. Dahmouche, "MiGriBot: A miniature parallel robot with integrated gripping for high-throughput micromanipulation," *Science Robotics*, vol. 7, no. 69, p. eabn4292, Aug 2022.

[7] V. Varma and W. Dixon, "Design of a piezoelectric meso-scale mobile robot: a compliant amplification approach," in *Proceedings 2002 IEEE International Conference on Robotics and Automation*, vol. 2. Washington, DC, USA: IEEE, May 2002, pp. 1137–1142.

[8] L. L. Howell, *Compliant Mechanisms*. John Wiley & Sons Ltd., 2001.

[9] J.-s. Koh, S.-p. Jung, R. J. Wood, and K.-j. Cho, "A jumping robotic insect based on a torque reversal catapult mechanism," in *2013 IEEE/RSJ International Conference on Intelligent Robots and Systems*. IEEE, Nov. 2013, pp. 3796–3801.

[10] A. Tabak and R. Orszulik, "A Monolithic Flexible Transmission for Piezoelectric Actuators," in *2022 IEEE/ASME International Conference on Advanced Intelligent Mechatronics (AIM)*, Sapporo, Japan, Jul 2022, pp. 138–143.

[11] P. A. York and R. J. Wood, "A geometrically-amplified in-plane piezoelectric actuator for mesoscale robotic systems," in *2017 IEEE International Conference on Robotics and Automation (ICRA)*, Singapore, Singapore, May 2017, pp. 1263–1268.

[12] A. Tabak, "Design and additive manufacture of a high-speed piezoelectrically actuated compliant mesoscale parallel robot," Master's thesis, York University, 2023.

[13] A. Parmiggiani, E. Ottonello, S. M. Kargar, M. Baggetta, G. Hao, and G. Berselli, "Deltaflex-an additively manufactured delta robot with compliant joints: Virtual prototyping and experimental evaluation," *Journal of Mechanisms and Robotics*, vol. 16, no. 11, p. 111011, July 2024.

[14] A. Raatz, J. Wrege, S. Soetebier, and J. Hesselbach, "High precision compliant parallel robot with an optimized large workspace," in *International Design Engineering Technical Conferences and Computers and Information in Engineering Conference*, vol. 28th Biennial Mechanisms and Robotics Conference, Parts A and B, Sept 2004, pp. 1007–1014.

[15] M. Leveziel, G. Laurent, M. Gauthier, and R. Dahmouche, "Modeling, analysis, and optimization of a miniaturized parallel robot with soft joints for high-speed real-time control," *Journal of Micro and Bio Robotics*, vol. 21, p. 8, May 2025.

[16] M. Naves, M. Nijenhuis, B. Seinhorst, W. Hakvoort, and D. Brouwer, "T-flex: A fully flexure-based large range of motion precision hexapod," *Precision Engineering*, vol. 72, pp. 912–928, Nov 2021.

[17] C. Gosselin and J. Angeles, "The Optimum Kinematic Design of a Planar Three-Degree-of-Freedom Parallel Manipulator," *Journal of Mechanisms, Transmissions, and Automation in Design*, vol. 110, pp. 35–41, Mar. 1988.

[18] Y. Lou, G. Liu, and Z. Li, "Randomized optimal design of parallel manipulators," *IEEE Transactions on Automation Science and Engineering*, vol. 5, no. 2, pp. 223–233, Apr 2008.

[19] J.-P. Merlet, *Parallel Robots*. Springer Dordrecht, 2006.

[20] D.-Y. Jo and E. J. Haug, "Workspace analysis of closed loop mechanisms with unilateral constraints," in *International Design Engineering Technical Conferences and Computers and Information in Engineering Conference*, vol. Mechanical Systems Analysis, Design and Simulation, Sept 1989, pp. 53–60.

[21] E. J. Haug, C.-M. Luh, F. A. Adkins, and J.-Y. Wang, "Numerical algorithms for mapping boundaries of manipulator workspaces," *Journal of Mechanical Design*, vol. 118, no. 2, pp. 228–234, Jun 1996.

[22] J. A. Snyman, L. J. du Plessis, and J. Duffy, "An optimization approach to the determination of the boundaries of manipulator workspaces," *Journal of Mechanical Design*, vol. 122, no. 4, pp. 447–456, Jul 1998.

[23] S. Agrawal, "Workspace boundaries of in-parallel manipulator systems," in *Fifth International Conference on Advanced Robotics 'Robots in Unstructured Environments*, Jun 1991, pp. 1147–1152 vol.2.

[24] V. Kumar, "Characterization of workspaces of parallel manipulators," *Journal of Mechanical Design*, vol. 114, no. 3, pp. 368–375, Sept 1992.

[25] D. Oetomo, D. Daney, B. Shirinzadeh, and J.-P. Merlet, "An interval-based method for workspace analysis of planar flexure-jointed mechanism," *Journal of Mechanical Design*, vol. 131, no. 1, p. 011014, Dec 2008.

[26] Z. Wang, S. Ji, Y. Li, and Y. Wan, "A unified algorithm to determine the reachable and dexterous workspace of parallel manipulators," *Robotics and Computer-Integrated Manufacturing*, vol. 26, no. 5, pp. 454–460, Oct 2010.

[27] K. G. Gim, J. Kim, and K. Yamane, "Design of a serial-parallel hybrid leg for a humanoid robot," in *2018 IEEE International Conference on Robotics and Automation (ICRA)*, May 2018, pp. 6076–6081.

[28] W. Haouas, R. Dahmouche, N. Piat, and G. Laurent, "A New Seven Degrees-of-Freedom Parallel Robot With a Foldable Platform," *Journal of Mechanisms and Robotics*, vol. 10, no. 4, pp. 1 – 15, Apr 2018.

[29] M. Mazare, M. Taghizadeh, and M. R. Najafi, "Kinematic analysis and design of a 3-dof translational parallel robot," *International Journal of Automation and Computing*, vol. 14, no. 4, p. 432–441, Mar 2017.

[30] R. E. W. Rafael C. Gonzalez, *Digital Image Processing*. Pearson Education Ltd., 2018.

[31] S. Suzuki and K. be, "Topological structural analysis of digitized binary images by border following," *Computer Vision, Graphics, and Image Processing*, vol. 30, no. 1, pp. 32–46, Apr 1985.

[32] C. Gosselin, "Kinematic analysis, optimization and programming of parallel robotic manipulators," Ph.D. dissertation, McGill University, 1985.

[33] C. Gosselin and J. Angeles, "Singularity analysis of closed-loop kinematic chains," *IEEE Transactions on Robotics and Automation*, vol. 6, pp. 281–290, Jun. 1990.